

Reconstructions of Pinhole Images in the Presence of Noise, with Application to Inertial Confinement Fusion Product Neutrons

C. R. Christensen, Cris W. Barnes, and T. J. Murphy

Los Alamos National Laboratory, Los Alamos, New Mexico, 87545

The problem of pinhole imaging is treated for the case in which resolution is dominated by statistical noise and the penetration of the pinhole substrate by the particles (neutrons or energetic X rays) being imaged. A method for reconstructing the source object by inverting the images is developed, using linear algebra, singular value decomposition, and constrained optimization. It is shown how the geometric factors of the set-up contribute to reconstruction quality. The geometry is found that produces the best reconstruction quality for a given yield and source test pattern. Signal to noise and resolution are quantified. The issue of reconstruction reliability is addressed. Examples are given for neutron images produced by ICF implosions.

PACS numbers: 52.57 -z, 07.05.Pj, 42.30.Wb

LA-UR-02-2616

I. Introduction

Apertures are used in imaging when a suitable refracting element cannot be found. This is certainly the situation in the cases of energetic X rays and neutrons. Aperture imaging involves the formation of an image on a detector by those particles or rays going through a hole in a material body. The body itself is often referred to as a “pinhole” or “aperture”, but is more correctly called an occluder – the aperture is the hole in the body.

The radius of the aperture used places the problem between two limits: pinhole¹ and penumbral^{2,3} imaging. The pinhole limit obtains when the relationship between aperture radius, detector element size, and the object and image distances is such that a single object point produces an image that is smaller than a detector element, or pixel. (It should be noted that, strictly speaking, the pinhole limit is unattainable when the radiation can penetrate or

scatter within the occluder.) In this case, there is a one-to-one relationship between object (source) and image points, and the image faithfully reproduces the object in two dimensions with no signal processing. The penumbral regime uses an aperture big enough that a point in the center of the detector has a clear path to every point in the entire object. Because every image point receives signal from many object points, the image must be mathematically inverted (unfolded) to give a reconstruction of the source.

Pinhole imaging is advantageous because it is accurate and has high resolution, but a pinhole transmits relatively little signal. Penumbral imaging has good signal level, but unavoidably magnifies statistical noise in the required reconstruction process. The optimal procedure to extract the maximum amount of information possible from a limited amount of signal must lie between these two extremes.

The principles of pinhole imaging were understood in the late 16th century.⁴ In this paper, we explore the issues that contribute to the resolution of an occlusive imaging system when there is a high level of noise on the signal, or when the particles of interest can penetrate through the occluder. We have developed an algorithm for image inversion based on direct calculation of probability distribution integrated over the areas of square detector pixels. For the case of neutron imaging, penetration of and scattering within the occluder are explicitly calculated. Two approximations are made: discretization of the source and neglect of multiple scattering in the occluder. These assumptions will be justified later. Because the problem is formulated in terms of matrices, the influence of geometric parameters on system performance can easily be explored using the concept of matrix conditioning⁵. A noise reduction algorithm has been developed using the process of singular value decomposition⁶ and constrained optimization. With these techniques in hand, we are in a position to find the

optimal geometry to maximize information-gathering ability for any given total signal input. It is shown that the amount of information one can retrieve can be greatly increased by doing mathematical reconstructions of the source object.

These techniques are widely applicable. Herein, they are illustrated with reference to imaging of laser-induced implosions of inertial confinement fusion (ICF) targets.⁷ Such implosions can give off X rays and fusion product neutrons, in amounts that make statistical noise the dominant factor in imaging resolution. Our source objects are small ($\sim 50 \mu\text{m}$ radius), but the techniques we develop are applicable to any scale.

In Section II, the geometry of the problem is presented and the free parameters defined. Section III explains how the problem is formulated in terms of matrices, defines condition number, and gives an illustration of its importance. We also give an intuitive explanation of how each free parameter affects the condition number. Section IV explains the noise reduction process. In Section V, we present the results of a scan of the free parameters in the problem to find the optimum geometry. An example reconstruction is given for a yield achievable in current experiments. Section VI addresses the topic of error bars on the reconstructions. The related subject of system resolution is treated. The summary (Section VII) deals with practical considerations of how these techniques are applied to an experimental situation.

II. Geometry

For the examples to be presented, the following geometry is used (Figure 1): r_o is the radius of the field of view in the object plane. The source is projected onto the object plane, at a distance ℓ_o from the aperture, which has radius r_a . The detector (image plane) is at a distance of ℓ_i from the aperture. w is the width of a pixel and n is the number of pixels across needed to contain the image. (Because of penetration, neutron images will not have a sharp cut-off. The radius r_i of the

image is taken as r_o times the magnification, l_i/l_o . The actual physical detector used to capture this image would of course be bigger.) The pixels in question might be the physical elements of a scintillator neutron detector¹, or the pores of a microchannel plate of an X-ray detector⁸. It might be desirable for a given problem to group together several physical detector elements as one pixel of the image analysis.

Figure 1 shows a thick occluder appropriate to neutron imaging. It is made of some dense material such as gold, so as to attenuate the flux of particles not going through the aperture. Because low-energy X rays are less penetrating, a simple hole in a thin plate is adequate.

The diagram is not drawn to scale; a realistic geometry might have an aperture radius less than 10 μ m, a detector radius of a few centimeters and a detector distance of several meters. The occluder probably would not extend all the way to the detector for practical reasons. Beyond the first few mean free paths, the extra material does not afford much additional attenuation.

The occluder shown is not top-to-bottom symmetric. The shape chosen presents the same clear aperture to every source point. The two inner cone angles are such that every ray beginning on a point in the object plane within a radius of r_o and ending on a point in the image plane within a radius of r_i is unobstructed. All other rays are cut off by as much metal as possible. The cone defining the outer surface is determined by the circles of radius r_o and r_i in the object and image planes respectively. If the occluder were allowed to extend outside this cone, neutrons that would have hit the image plane *outside* a radius of r_i if they were undeflected might scatter *into* the detector. Previous designs have tried to maximize a quality called isoplanarity⁹, which means that the image would be the same for all source points, regardless of their position in the object

plane. This is not of concern to us because we are doing exact calculations, and do not use this approximation.

If r_o is defined by the problem (about 50 μ m for an ICF capsule), the free parameters are ℓ_o , r_a , and n . ℓ_i is dependent: $\ell_i = \ell_o n w / 2r_o$. w is a free parameter in the code developed in this paper, but in what follows, w is set at 1 mm, because this is typical for scintillator neutron detectors. Section IV introduces a fourth free parameter: the number of eigenvectors used in the decomposition of the matrix.

III. Matrix representation

Any discrete linear transformation can be written in matrix form. An apparently different method will be reducible to matrix form as long as it's linear. We write this explicitly: $\mathbf{M}\mathbf{o} = \mathbf{i}$, where \mathbf{o} is the object and \mathbf{i} is the image. Since \mathbf{o} and \mathbf{i} are both two-dimensional, \mathbf{M} should be four dimensional, but if we concatenate the rows of \mathbf{o} and \mathbf{i} to form column vectors, \mathbf{M} will be two dimensional, with each column representing the image produced by one source point. \mathbf{M} is an $N \times N$ array, where $N < \lfloor (n / 2) \rfloor^2$. Equality does not hold because the pixels at the edge, which are only partially illuminated, are omitted. The source is modeled as the sum of N delta functions, situated at the points that are the reflections through the center of the aperture of the centers of the detector pixels. N independent pieces of information are the most we can hope to ask for under ideal circumstances. Discretization is justified when we are not asking for a level of detail in the inversions finer than the extent of several pixels. We shall see later what happens when this is violated.

\mathbf{M} is split up into three contributions: $\mathbf{M} = \mathbf{M1} + \mathbf{M2} + \mathbf{M3}$. $\mathbf{M1}$ comprises particles (neutrons or photons) that pass through the aperture and never hit the occluder. $\mathbf{M2}$ accounts for particles penetrating through the occluder along straight-line paths. This flux is attenuated by the amount of metal between any pair of object and image points. $\mathbf{M3}$ includes particles that are scattered once in

the occluder but still hit the detector. Multiple scattering is neglected. (This is justified below.)

$\mathbf{M1}_{jk}$ is the direct contribution to the pixel centered at $(x_j, y_j, -\ell_i)$ from the source point at (x_k, y_k, ℓ_o) . It is the quantity

$$\frac{dx dy (\ell_o + \ell_i)}{4 \sqrt{[(x - x_k)^2 + (y - y_k)^2 + (\ell_o + \ell_i)^2]^{3/2}}$$

integrated over the area of the square pixel.

$$\frac{dx dy}{4 \sqrt{[(x - x_k)^2 + (y - y_k)^2 + (\ell_o + \ell_i)^2]}$$

is the fraction of solid angle subtended, and

$$\frac{\ell_o + \ell_i}{\sqrt{[(x - x_k)^2 + (y - y_k)^2 + (\ell_o + \ell_i)^2]^{1/2}}$$

is the cosine of the angle to the normal. The projection of the aperture onto the image plane is round, so for some pixels, the integration is only up to the edge of this shadow.

$\mathbf{M2}_{jk}$ has the same integrand, but multiplied by $\exp(-d_{jk}/\lambda)$, where d_{jk} is the distance a particle must travel through metal to get from (x_k, y_k, ℓ_o) to $(x_j, y_j, -\ell_i)$. λ is the mean free path for neutrons in the metal: $\lambda = 1 / \Sigma_{\text{tot}} n$, where Σ_{tot} is the total cross section for scattering, and n is the number density. The material used in the examples in this paper is gold. All nuclear data come from the Brookhaven ENDF/B-VI 300 K library¹⁰. $\mathbf{M2}$ is zero for the pixels lying in the unshadowed area. For pixels straddling the shadow edge, the integration is over the complements of the pieces included in $\mathbf{M1}$.

The matrix $\mathbf{M3}$ accounts for scattering in the occluder. Various processes can contribute to scattering; however in this case, three are dominant. The cross section for elastic scattering of 14.1 MeV neutrons by gold is $\Sigma = 2.64$ barns. The $(n, 2n)$ reaction has $\Sigma = 2.13$ barns, and $Q = -8.06$ MeV. The (n, n') continuum

contribution is $\sigma = .468$, with $Q = -.0995$ MeV. Together these three account for 99% of the total cross section of 5.31 barns.

The calculation of elastic scattering is described first.

Neutrons are emitted isotropically into 4π steradians from a source point (x_k, y_k, ℓ_o) . For some emission angles θ and ϕ , the undeflected ray will pass through the metal. From entrance point to exit point of the undeflected ray, a particle emitted at these angles has a probability of scattering at any intermediate point proportional to $\exp(-d_{in} / \lambda_{in})$, where d_{in} is the distance from entrance point to scattering point, and λ_{in} is the mean free path for 14.1 MeV neutrons. This is because the flux has been attenuated by this factor. The particles have not simply disappeared; they have been *scattered out* of this path. The majority do not hit the detector. Those that do are included in M3. The probability that a neutron scattered at the point of interest hits the detector is proportional to the differential scattering cross section for the angle defined by the initial path and the ray from the scattering point to the image point $(x_j, y_j, -\ell_i)$. The neutron must still exit the metal, so its probability is multiplied by $\exp(-d_{out} / \lambda_{out})$, where d_{out} is the distance through the metal from scattering point to exit point, and λ_{out} is the mean free path for the neutron at the lower energy produced by scattering. For realistic geometry, an elastically scattered neutron that hits the detector must have been deflected at a very shallow angle. Shallow angle scattering of a neutron off gold doesn't change the energy appreciably, so $\lambda_{out} = \lambda_{in}$ to high precision. Again, the flux is attenuated on the way out because particles are scattered out of the path. Most do not hit the detector. Those that do have been multiply scattered and are neglected in this calculation. The probability for each pair of object and image points is now integrated over emission angles θ and ϕ , path distance d_{in} , and the area of the pixel in the image plane.

The (n, 2n) reaction produces a smaller detected response than an elastic reaction with the same scattering cross section for two reasons, both having to do with the net loss of 8 MeV, and the division of the remaining 6 MeV between the two neutrons. The first effect is a decrease of the mean free path. Between 6 keV and 6 MeV, the total cross section is higher than it is for 14 MeV neutrons, so the flux is attenuated more as it exits the metal. The second effect comes about because the response of the scintillator scales roughly as the three-halves power of energy.¹¹ Thus a neutron of a given energy produces a bigger signal than two neutrons whose energies sum to the original amount. The (n, n γ) continuum interaction also involves a loss of energy to the scattered neutron.

M3 is calculated by summing together the three differential cross sections at each angle, but neglecting the decrease of energy of the inelastically scattered particles. This produces an overestimate of the total effect of scattering. Even so, it is found that for realistic occluder dimensions ($nw \ll \ell_i$), **M3** is small (<1% of **M1**). This justifies the neglect of multiple scattering. Because **M3** takes a long time to calculate, it is often omitted in the examples that follow. For a given experimental situation, it should probably still be calculated in order to make sure it's negligible for that specific geometry.

For low energy X rays, only **M1** is calculated. For higher energy X rays, the issue of penetration might have to be addressed.

Figure 2 a, b, and c show the components of **M1**, **M2**, and **M3** produced by a single source point for $n = 30$, $\ell_o = 3$ cm, and $r_a = 6$ microns. **M3** has been rescaled by 3.5×10^3 to be more visible. Figure 2d shows the component of $\mathbf{M} = \mathbf{M1} + \mathbf{M2} + \mathbf{M3}$. These form one column of the matrices (response to one source point). They are turned from column vectors back into square arrays, so what is seen is the probability distribution produced in the image plane by one source point. Notice that **M3** is centered about the axis of the occluder, not the center of the

direct image ($\mathbf{M1}$). The white circle shows the edge of the shadow of the aperture, projected onto the image plane. Also shown at the bottom of Figure 2 is the normalized color scale used in all diagrams in this paper. The normalization used when displaying \mathbf{M} is approximately equal to the fraction of solid angle subtended by one pixel, or $w^2 / 4\pi(\ell_o + \ell_i)^2$. This is of the order of 10^{-10} to 10^{-8} . When \mathbf{o} is displayed, the scale is appropriate to the particle yield. The normalization for \mathbf{i} is roughly equal to the product of the two.

Figure 3 shows all the columns of \mathbf{M} . The response to one source point, such as that shown in Figure 2d, is made into a column vector by placing the rows end-to-end. (Only those pixels lying completely within a radius of r_i are included. This causes a variation in the width of the bands.) The column of Figure 2d is shown on the right, and the arrow indicates its place in the matrix.

If detector imperfections are known, the point spread functions can be put into a separate matrix that left-multiplies \mathbf{M} . This would give the expected signals after detection.

The calculations have been done for deuterium-tritium fusion neutrons only. Deuterium-deuterium fusion produces a lower energy neutron with a shorter mean free path, which would give a narrower point spread function. However, DD experiments have not so far produced a yield high enough to image.

We now turn to the question of how we should choose the dimensions of the problem. We shall see that there are some good choices and some poor ones. The two factors that determine the amount of information that can reliably be extracted from the data are matrix conditioning and particle throughput. It must be stressed that the concept of conditioning is herein stated in terms of linear algebra, but the concept is perfectly general. For example, it is not difficult to show that analysis by Fourier decomposition is easily rewritten in terms of matrices. Using matrices directly makes the concepts more easily apparent.

The fundamental problem arises from the overlapping in the responses from neighboring source points that comes about when the aperture is enlarged to increase particle throughput. No matter the formalism of the unfold process, one way or another, subtraction must be performed to separate the responses of the individual points. With matrices, this takes the form of Gaussian elimination. Any subtraction that is done is deleterious, because the entries subtract, *but the noise adds in quadrature!* A small amount of noise on the image can be greatly magnified in the reconstruction, producing meaningless results. An example is shown in Figure 4 for two different choices for the dimensions in the problem. The first represents an extreme example of penumbral imaging ($n = 40$, $w = .5$ mm, $r_a = 1000$ μ m, $r_o = 3.8$ cm, $\ell_o = 1$ cm). The test object is shown in panel a). This is an unrealistic shape for an ICF capsule, but the sharp edges are a stringent test of the unfolding. Panel b) shows the image produced by converting the object to a column vector, multiplying by \mathbf{M} , and converting back to a square array. Panel c) is the reconstruction produced from $\mathbf{o} = \mathbf{M}^{-1}\mathbf{i}$. It's not exactly like the object because of discretization. Panel d) shows the image with a small amount of noise added, and e) shows the reconstruction. A small amount of noise has been magnified by the poorly conditioned matrix to give useless results. Parts f) and g) show a reconstruction for the pinhole case ($n = 40$, $w = 1$ mm, $r_a = 1.5$ μ m, $\ell_o = 1$ cm, $r_o = 100$ μ m. The aperture is smaller and ℓ_o / r_o is larger.) Panel f) is the image produced by the same test pattern with the new geometry, and g) is the reconstruction. The noise is not magnified, because the matrix is well conditioned. Only the $\mathbf{M}\mathbf{1}$ (direct) component is used here, which gives too favorable a representation of pinhole imaging for neutrons. The examples were chosen to illustrate the concept of conditioning and show some of the factors involved.

Figure 5 is a representation of the matrices used in the previous example. (Only small blocks of the larger matrices are shown.) The entries are represented by colors. It is seen in a) that the poorly conditioned matrix (penumbral case) requires subtractions, whereas the well conditioned matrix in b) (pinhole case) is diagonal. This is because the response to one source point is covered by only one pixel.

Matrix conditioning is quantified by the condition number⁵. For a symmetric matrix, it is defined as

$$c = \lambda_{\max} / \lambda_{\min}$$

where λ_{\min} and λ_{\max} are the smallest and largest eigenvalues of the matrix.

For realistic geometry, \mathbf{M} is almost symmetric. There is another, less simple formula to be used in the general case, and the special case approaches the general continuously. For purposes of illustration, the simpler formula appropriate to the symmetric case is used.

Recall that eigenvalues λ are defined in terms of their corresponding eigenvectors \mathbf{v} : $\mathbf{M}\mathbf{v} = \lambda\mathbf{v}$. These are vectors whose direction is unchanged upon multiplication by \mathbf{M} . An example in this context is the constant vector, which is almost an eigenvector. In the limit that $nw \ll \ell_i$, a uniform illumination of the field of view would produce a uniform image.

The matrix in Figure 5a) has a condition number of 2.2×10^5 and that in 5b) is 1.0001. The significance of the condition number can be understood as follows. A small amount ϵ_i of noise on the image produces some amount of noise on the reconstructed object.

$$\mathbf{M}\mathbf{o} = \mathbf{i} \text{ and } \mathbf{M}(\mathbf{o} + \epsilon\mathbf{b}) = \mathbf{i} + \epsilon\mathbf{i}$$

so $\mathbf{M}\epsilon\mathbf{b} = \epsilon\mathbf{i}$ because the system is linear.

All the eigenvalues of \mathbf{M} are positive, so $\|\mathbf{i}\| = \|\mathbf{M}\mathbf{o}\| \leq \lambda_{\max} \|\mathbf{o}\|$ and

$\|b\| = \|M o\| \geq \sigma_{\min} \|o\|$. The double bars represent length in the usual sum of squares sense. It follows immediately that

$$\frac{\|b\|}{\|o\|} \leq c \frac{\|i\|}{\|i\|}.$$

This means that the fractional noise on the data can be multiplied by a very large number during reconstruction, so the goal is to keep c small to guarantee a good reconstruction. What geometric properties keep c small? From Figure 4 it is apparent that a small aperture is desirable. For neutrons, as ℓ_o increases, there is more metal to go through, so the point spread function (see Figure 2) narrows, the matrix becomes more nearly diagonal, and c goes down. For X-rays, the only requirement is that $\ell_o \gg r_o$, or equivalently, $\ell_i \gg nw$. This makes all the diagonal entries nearly equal, so the eigenvalues are nearly equal, and c is small. (Think of a diagonal matrix, where the eigenvalues appear along the diagonal.)

Thus we see that having small r_a and big ℓ_o decreases noise magnification, but it also cuts down the signal level, meaning there is a higher fractional noise to start with. Having n small and w big decreases c , because the response to one source point covers few pixels, so little subtraction is necessary. However, it also limits the resolution achievable if there were no noise. What is needed is systematically to scan parameter space to find the optimum. This is presented in Section V.

Section IV: Noise Reduction

When there is limited signal amplitude, we must be prepared to sacrifice condition number to some extent for the sake of particle throughput. Is there some way to reduce the noise thus introduced? The subject is familiar in Fourier analysis. Using that method, one discards or reduces the amplitude of the highest frequencies. This is ideal for a system described by a second order linear differential equation with constant coefficients, because a sinusoid is an

eigenmode. For our problem, c can be decreased by discarding eigenvectors. We want to start with the smallest eigenvalues. Small eigenvalues are bad because just a little noise on \mathbf{i} in the direction of the corresponding eigenvector will be inverted to a large amount of noise on \mathbf{o} . (Small eigenvalues of \mathbf{M} correspond to large eigenvalues of \mathbf{M}^{-1} , while the eigenvectors are the same.) Figure 6 shows the “best” (highest eigenvalued) and “worst” (lowest eigenvalued) vectors for the same \mathbf{M} shown in Figure 3. (Remember that the N -element vectors have been put back into $n \times n$ arrays in Figure 6.) The lowest order vector has a positive average value. It is normalized so that black is zero and red is one. The others have zero average value, and they are normalized so that blue-green is zero.

We use the formal procedure of singular value decomposition (SVD) to produce a new matrix \mathbf{M} made up of only the vectors we choose. (The column space of \mathbf{M} is being restricted, producing a singular matrix, which is uninvertible. SVD gives us a way to “invert” \mathbf{M} producing the pseudo-inverse, or Moore-Penrose generalized inverse. The vectors that are discarded by SVD are actually eigenvectors of $\mathbf{M}^T\mathbf{M}$, but because \mathbf{M} is almost symmetric, they will be close to the eigenvectors of \mathbf{M} . The important point is that they form a complete basis for the space of $N \times N$ matrices, and the ones with the lowest eigenvalues have the highest spatial frequencies. A possible alternative would be to find \mathbf{M}^{-1} , then discard *its* eigenvectors, but SVD is computationally simpler. See Reference 5.)

The “worst” ones are discarded first. The number m of vectors retained is the fourth free parameter (along with r_a , n , and ℓ_o).

Using SVD with successively fewer vectors fits the data with progressively smoother reconstructions with less and less information. However, we are not yet using all the information available. Negative entries in the reconstruction are unphysical, so it is appropriate to set them to zero. But there is information contained in those negative elements. A negative value in \mathbf{o} , the reconstructed

object, must have been caused by noise in \mathbf{i} . If we adjust the value of the pixel in \mathbf{i} considered most likely to have caused the problem, it will also change other elements of \mathbf{o} that might not have been negative. Thus this information can be used rather than simply discarded.

The two approaches can be combined. That is, the elements of \mathbf{o} are adjusted to maximize the conditional probability of \mathbf{i} given \mathbf{o} , $P(\mathbf{i}|\mathbf{o})$, subject to the constraint that \mathbf{o} must be non-negative. Rather than using \mathbf{M} to calculate $\mathbf{M}\mathbf{o}$, $\mathbf{M}\square$ is used, with the chosen number of retained vectors. We started out using the Poisson distribution to calculate $P(\mathbf{i}|\mathbf{o})$, and adjusting \mathbf{o} to maximize it. However, it was found that, for test patterns, this didn't give reconstructions as good as those obtained by minimizing $\|\mathbf{M}\square - \mathbf{i}\|$, subject to the same constraint. The reason for this is not understood. For now, we use the latter method in our code.

Figure 7 gives an example for 10^{16} particles, $n = 26$, $\ell_o = 22$ cm, $r_a = 4$ \square m, $r_o = 50$ \square m, and $w = 1$ mm. The test pattern is shown in a), while b) is the inverted object with no noise reduction. The reconstruction shown in c) has been made non-negative using constrained optimization with all 476 eigenvectors retained. The remainder have 239, 170, and 21 vectors retained. 170 produce the minimum sum of squares error between the reconstruction and the original test pattern, and would be the choice for $\mathbf{M}\square$. Each panel of Figure 7 was scaled independently. With no noise reduction, the reconstruction goes both positive and negative. The zero value is thus blue-green for b), but black for the other panels.

Section V: Optimization

There is a design trade-off between matrix conditioning and particle throughput. In this section, the optimal geometry is found for a given yield and test pattern.

The test pattern shown in the first panel of Figure 8 was used to find the best reconstruction by varying the four free parameters (n , r_a , ℓ_o , and the number m of vectors). The total yield into 4π steradians was 8×10^{13} , which is presently achievable for direct drive capsules¹² at the Omega laser facility¹³ at the University of Rochester. The detector efficiency was taken to be 15%, which gives an equivalent yield of 1.2×10^{13} . The parameters were systematically scanned. For each choice, a reconstruction was formed from a noisy image and compared to the test pattern. The best reconstruction was found for $n = 30$, $r_a = 4.3 \mu\text{m}$, $\ell_o = 11.6 \text{ cm}$, and $m = 31$. A reconstruction employing these parameters is shown in Figure 8. It should be noted that this was not a sharp optimum, in that different choices close to this one produced reconstructions almost as good. The amount of variation in the parameters that causes $\|\mathbf{M}\mathbf{o} - \mathbf{i}\|$ to increase by 20% can be expressed as an uncertainty: $r_a = 4.3 \pm .7 \mu\text{m}$, $\ell_o = 11.6 \pm 1.6 \text{ cm}$, and $m = 31 \pm 2$. (The \pm signs should not be construed as denoting deviation in the formal sense.) $n = 26$ and $n = 28$ both produced reconstructions that were within 20% as good as those using $n = 30$. (The parameters were scanned only for even n .)

The magnification for the foregoing geometry is 300. This might not be practical for a given experimental situation. If there are constraints, such as how close the occluder can be to the implosion, the optimum would be found by scanning the allowed parameter space.

Up until this time, we have modeled the object as a sum of delta functions located at the centers of the pixels reflected onto the object plane. Now we calculate the response in the image plane to a source at an *arbitrary* point in the object plane, and then invert the image using \mathbf{M}^{-1} , which was calculated assuming all the object points were on the grid. This causes artifacts, even when there is no statistical noise. Figure 9 demonstrates this for $n = 26$, $w = 1 \text{ mm}$, $r_a = 4$

Δm , $\ell_o = 60$ cm, and $r_o = 50$ μ m. a) shows the image with no noise. b) shows the reconstruction. The original object points are shown as crosses. Notice the artifacts, some of which have negative values. c) shows the reconstruction with noise reduction. The ideal would be for the pixel where the object point lies to have the highest value, and adjacent pixels to have values proportionate to the inverse distance between the source point and the centers of those pixels. The reconstruction with noise reduction closely approaches this ideal. It can be concluded that the discretization of the problem is justified.

Section VI: Uncertainty estimates

Any time there is random noise in a system, information is lost. The procedure outlined above involves a further sacrifice of information as the eigenvectors are discarded to reduce noise. This is a worthwhile trade-off if the immunity to noise is enhanced, so that the information that is left is reliable. In this section, a method is outlined to quantify the reliability of the reconstructions. An example is shown in Figure 10 for $n = 24$, $r_a = 30$ μ m, $\ell_o = 21.5$ cm, and $r_o = 50$ μ m. a) shows the test object. The image is produced, and an ensemble of twenty different random noise sets is created for 10^{15} particles. One of the twenty is shown in b). The noisy images are inverted and noise reduction is applied. The mean and deviation for the twenty results are plotted in c) at the positions of the centers of the pixels, for a row of pixels just below $y = 0$. The signal to noise is taken to be the mean of the ratios of the values to the error bars at the highest third of the values. (This might be considered optimistic, but including S/N at the low values would give a meaninglessly low value.) S/N is 39 for this example.

Notice in b) that there seems to be no evidence of the dip in the center. In the reconstructions, this information is recovered. Reconstruction is not of much

advantage when the point spread function is narrow (Figure 4, f and g), but with neutrons, the PSF is *never* narrow, and reconstruction gives significant benefit.

If radius or ellipticity is the quantity of interest, a smaller error bar is obtainable. For the system geometry of the last example, we use as test pattern the greater of $k(1 - (r/30)^2)$ and zero. r is in microns and k normalizes the object to a yield of 10^{15} . The measured radius $r = \sqrt{\sum_j r_j^2 o_j / \sum_k o_k}$ for this test pattern is 17.30 μm . Next, twenty images with random Poisson-distributed noise are formed, and the reconstructions computed. The signal to noise for the individual pixels as computed above is 23.3. The measured radius is $17.38 \pm .04 \mu\text{m}$, which gives a S/N of 389.

The next test pattern is the greater of $k(1 - (x^2/a^2 + y^2/b^2))$ and zero, where $a = 30 \mu\text{m}$, $b = 20 \mu\text{m}$, and k normalizes the yield to 10^{15} . The measured ellipticity is $b/a = \sqrt{\sum_j y_j^2 o_j / \sum_k x_k^2 o_k} = 0.673$. For reconstructions of twenty noisy images, the S/N for the individual points is 16.7, whereas the measured ratio b/a is $0.676 \pm .002$, which is a S/N of 271.

A typical figure of merit for an imaging system is its resolution. The term has been variously defined. Here it is defined as twice the average rms width of the reconstructions of an ensemble of noisy images produced by point source objects (rms width = $\sqrt{\sum_j r_j^2 o_j / \sum_k o_k}$). Resolution will thus be a function of yield. For the example of Section V ($n = 30$, $r_a = 4.3 \mu\text{m}$, $\ell_o = 11.6 \text{ cm}$, and $m = 31$), the resolution is 9 μm for point sources of 10^{12} particles. In this test, the fifteen point source objects were placed randomly in the object plane. They were not on the grid of points formed by the projection through the aperture of the centers of the detector pixels, so there were reconstruction artifacts, as well as the statistical noise appropriate to the stated yield.

A different measure is the two-point resolution. This is the minimum distance in the object plane of two point sources that can barely be resolved in the reconstructions. If the reconstruction of a sum is equal to the sum of the reconstructions, two-point resolution should be roughly equal to one-point resolution. Examination of Figure 10 leads us to believe that the reconstruction of a sum is not equal to the sum of the reconstructions – there is a systematic error at the center, which is too high. There is no systematic error at the outside flanks of the curves, which suggests that if only one point source were used, there would be no systematic error. For practical purposes, this is probably not important, and the one-point and two-point resolutions both give the information one wishes to know.

A more typical scenario involves wanting to resolve two features, each of which has some spatial extent, which are superimposed on the signal from the rest of the object. All of these signals are in turn superimposed on the noisy background typical of the environments in which these measurements are made. It is hard to imagine one number that could be specified *a priori* that would give the information one wishes to know: how reliable is a reconstruction that seems to show particular distinct features? If one is expecting certain features, does a reconstruction that does not show them constitute a negative result? In general, one must do simulations in order to answer these questions. Figure 11 shows reconstructions of twelve noisy images, using the test pattern of Figure 8, the geometry of Section V, a yield of 8×10^{13} , and a detector efficiency of 15%. We conclude that the reconstructions are reliable in this case.

Section VII: Summary

In designing an experiment by the procedure put forth above, one first chooses a test pattern of a size, shape, and yield similar to what one expects for the planned experimental scenario. For example, if one wants to study neutron

emission from a failed ICF implosion, a theoretical simulation of that failure mode would be used. The parameters of the system will be chosen by minimizing $\|\mathbf{M}\mathbf{d} - \mathbf{i}\|$, as explained above. Alternatively, resolution or S/N might be used as the figure of merit.

The occluder will then be constructed. This paper has provided the tools to explore the question of whether or not it's worthwhile to build several occluders for different expected yields, or whether just one can give adequate performance for a range of results. One can know beforehand how much signal quality one has to sacrifice for the sake of practical issues concerning occluder fabrication.

The next step is to take the data, invert them, and apply noise reduction. Uncertainty is ascertained by forming a test pattern that reproduces the essential features of the reconstruction. Alternatively, the reconstruction itself could be used as the test pattern. Next an ensemble of noisy test images is formed whose noise level matches the data. Background noise should be added as well as the statistical noise from the direct neutron signal. Each of the simulations is reconstructed and compared to the others to gauge the uncertainty in the original reconstruction of the data. This was shown in Figure 11, using Poisson statistics to model the noise. Background noise and detector imperfections have not been taken into account in these simulations, because the appropriate level depends on the details of the specific experiment. An analysis of experimental data obtained at the Omega facility will be presented in an upcoming publication.

This work was performed under the auspices of the U. S. Department of Energy by the Los Alamos National Laboratory under contract number W-7405-Eng-36.

¹ Morgan, G. L., Berggren, R. R., Bradley, P. A., Cverna, F. H., Faulkner, J. R., Gobby, P. L., Oertel, J. A., Swenson, F. J., Tegtmeier, J. A., Walton, R. B., Wilke, M. D., Wilson, D. C., Disdier, L., Review of Scientific Instruments, vol. 72, No. 1, pp. 865-868.

-
- ² Lerche, R. A., Ress, D., Ellis, R. J., Lane, S. M., Nugent, K. A., *Laser and Particle Beams*, Vol. 9, No. 1, pp. 99-118.
- ³ Garconnet, J. P., Delage, O., Schirmann, D., Bertin, A., Grenier, G., Guilpart, B., Rouyer, A., *Laser and Particle Beams*, Vol. 12, No. 3, pp. 563-571, 1994.
- ⁴ G. della Porta, *Magiae Naturalis*, published 1611 but cited earlier.
- ⁵ *Linear Algebra and Its Applications*, Gilbert Strang, Academic Press, 1980, Sec. 7.2.
- ⁶ *op. cit.*, Sec. 3.4.
- ⁷ Lindl, J. D., and Cray, M., *Physics Today*, v. 48, No. 10, pp 104-104, Oct 1995.
- ⁸ Oertel, J. A. *et. al.*, *Laser and Particle Beams* (1991), vol. 9, no. 1, pp. 49-69.
- ⁹ Nugent, K. A., Luther-Davies, B., *Journal of Applied Physics*, Vol. 58, No. 7, pp. 2508-2515.
- ¹⁰ "Data Formats and Procedures Manual for Evaluated Nuclear Data File, ENDF-6", ENDF-102 (BNL-NCS-44945).
- ¹¹ Knoll, Glenn F., *Radiation Detection and Measurement*, John Wiley and Sons, 1979, Ch. 15, Sec III.
- ¹² Christensen. C. R. *et. al.*, to be published.
- ¹³ Boehly, T. R., Craxton, R. S., Hinterman, T. H., Kelly, J. H., Kessler, T. J., Kumpan, S. A., Letzring, S. A., McCrory, R. L., Morse, S. F. B., Seka, W., Skupsky, S., Soures, J. M., Verdon, C. P., *Review of Scientific Instruments*, Vol. 66, No. 1, 1995, pp. 508-510.

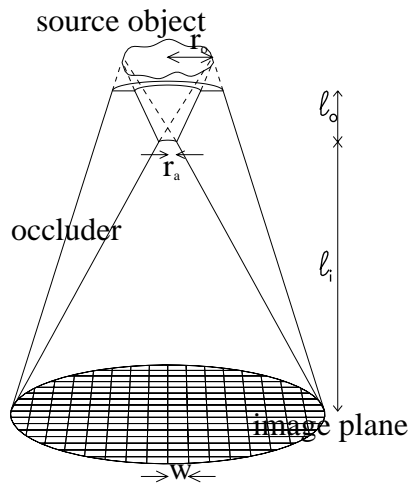


Figure 1: Occluder geometry

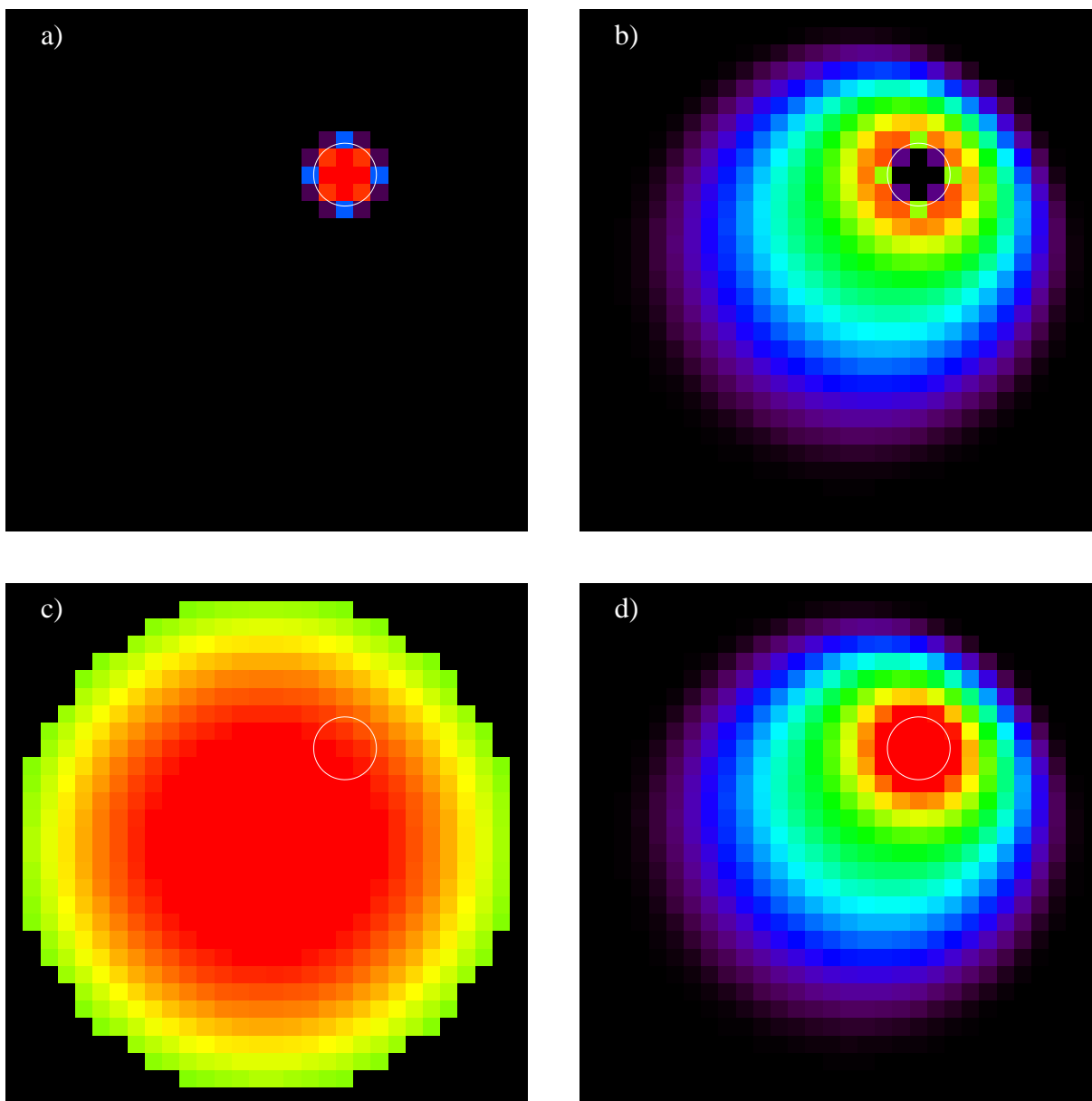


Figure 2: Probability of response in the image plane to a unit point source

a) M1 (direct neutrons)

b) M2 (penetrating neutrons)

c) M3 (scattered neutrons) $\times 3.5E3$

d) $M = M1 + M2 + M3$

The white circle shows the edge of the aperture projected onto the image plane, along a line passing through the source point and the center of the aperture

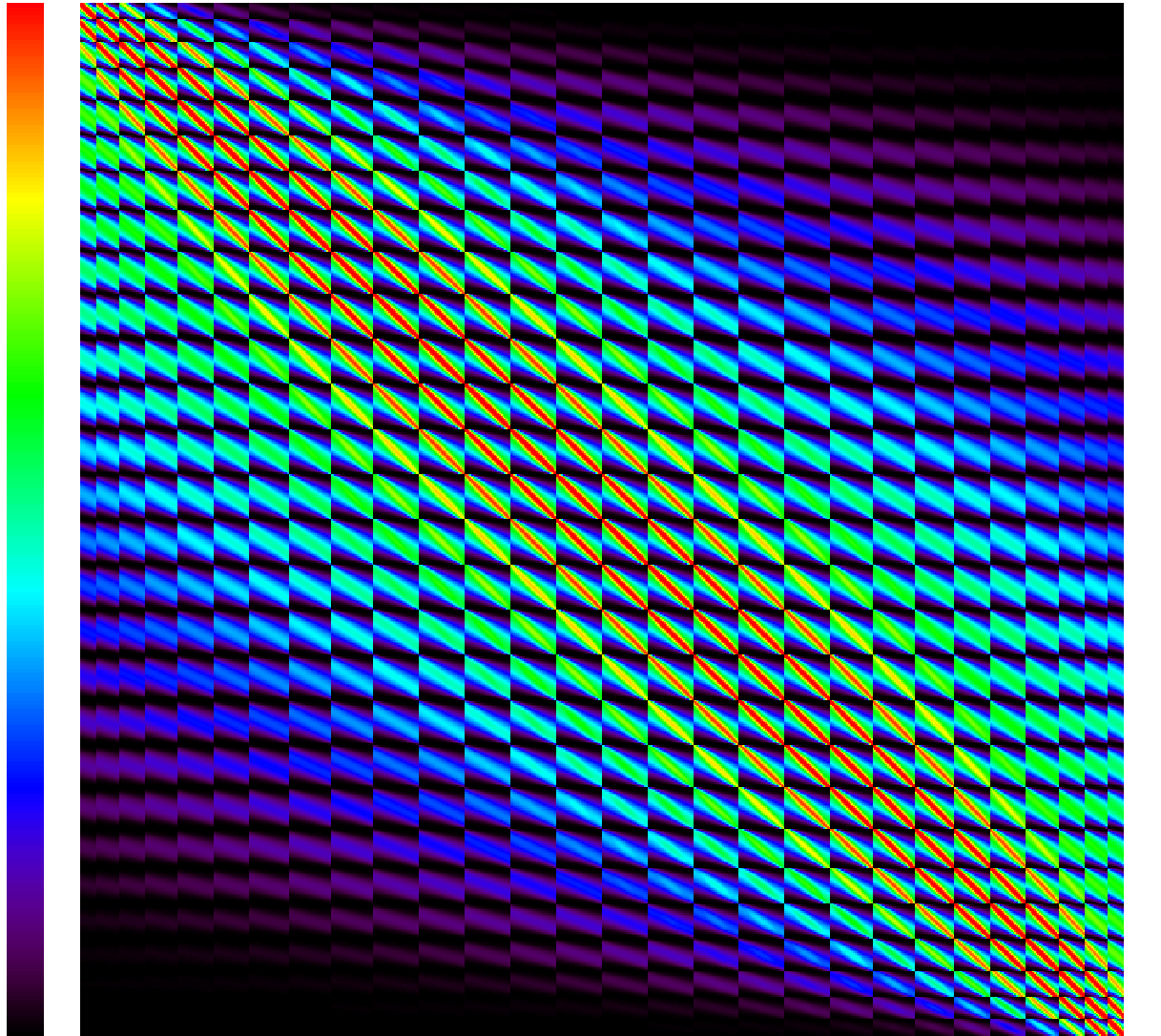
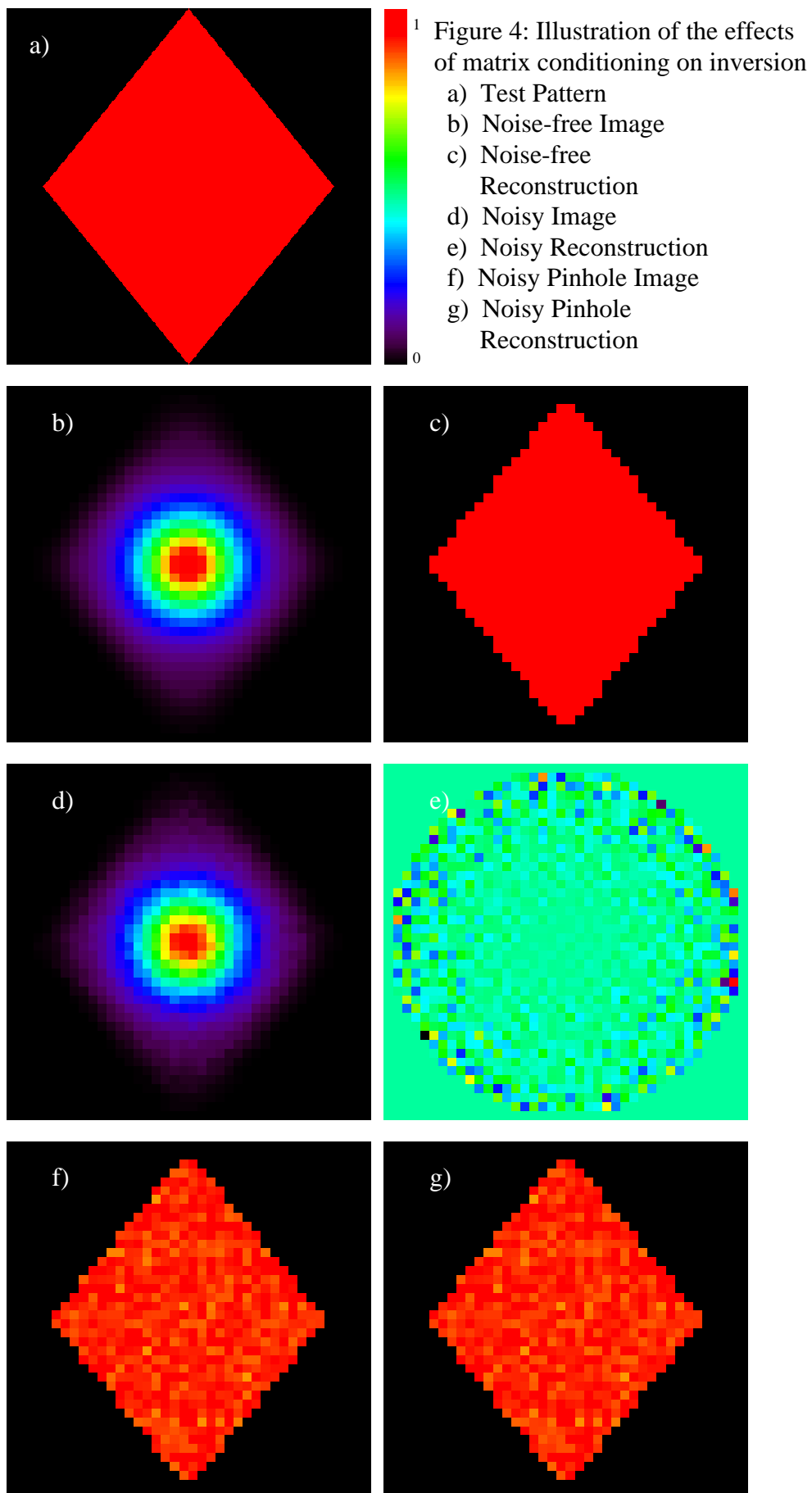


Figure 3: Representation of the entire matrix
for example of Figure 2
Color scale is on the left (0 to 9.76×10^{-10})
Figure 2d columnized on right (widened for visibility)
Arrow shows position of this column in matrix.



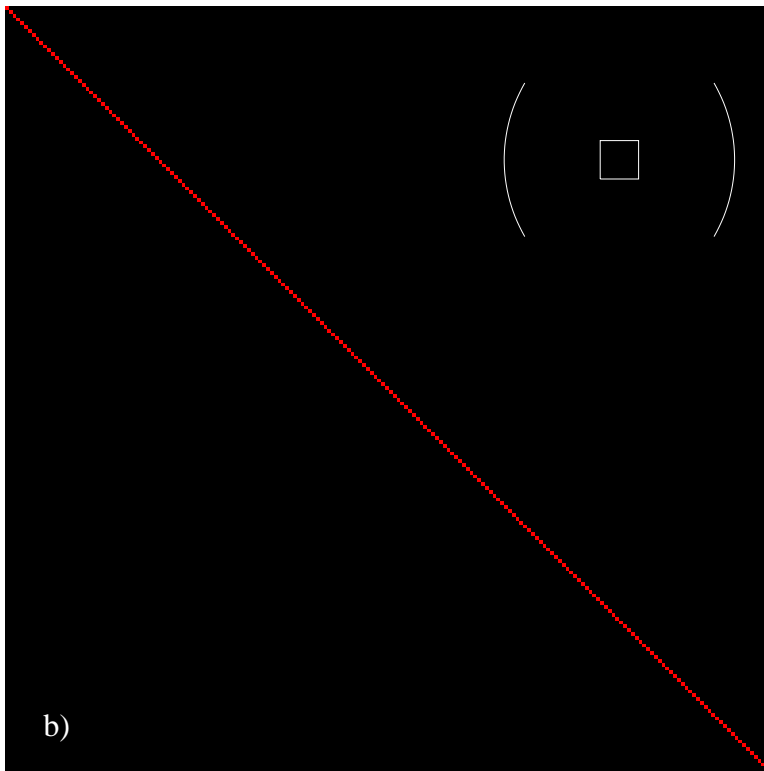
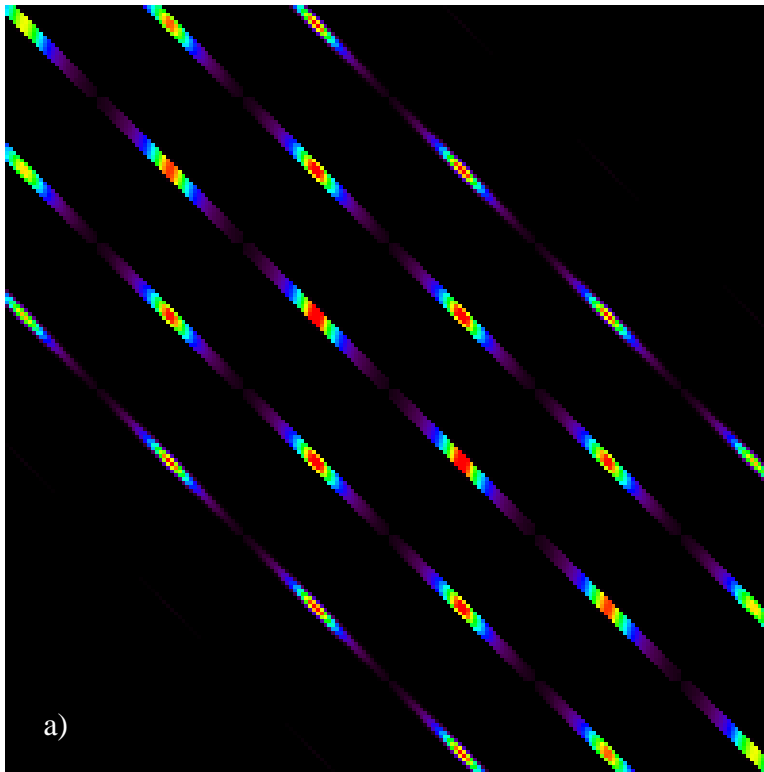


Figure 5: Bad and good matrix conditioning

a) Block from matrix shown in Figure 4 b-e

b) Block from matrix shown in Figure 4 f-g



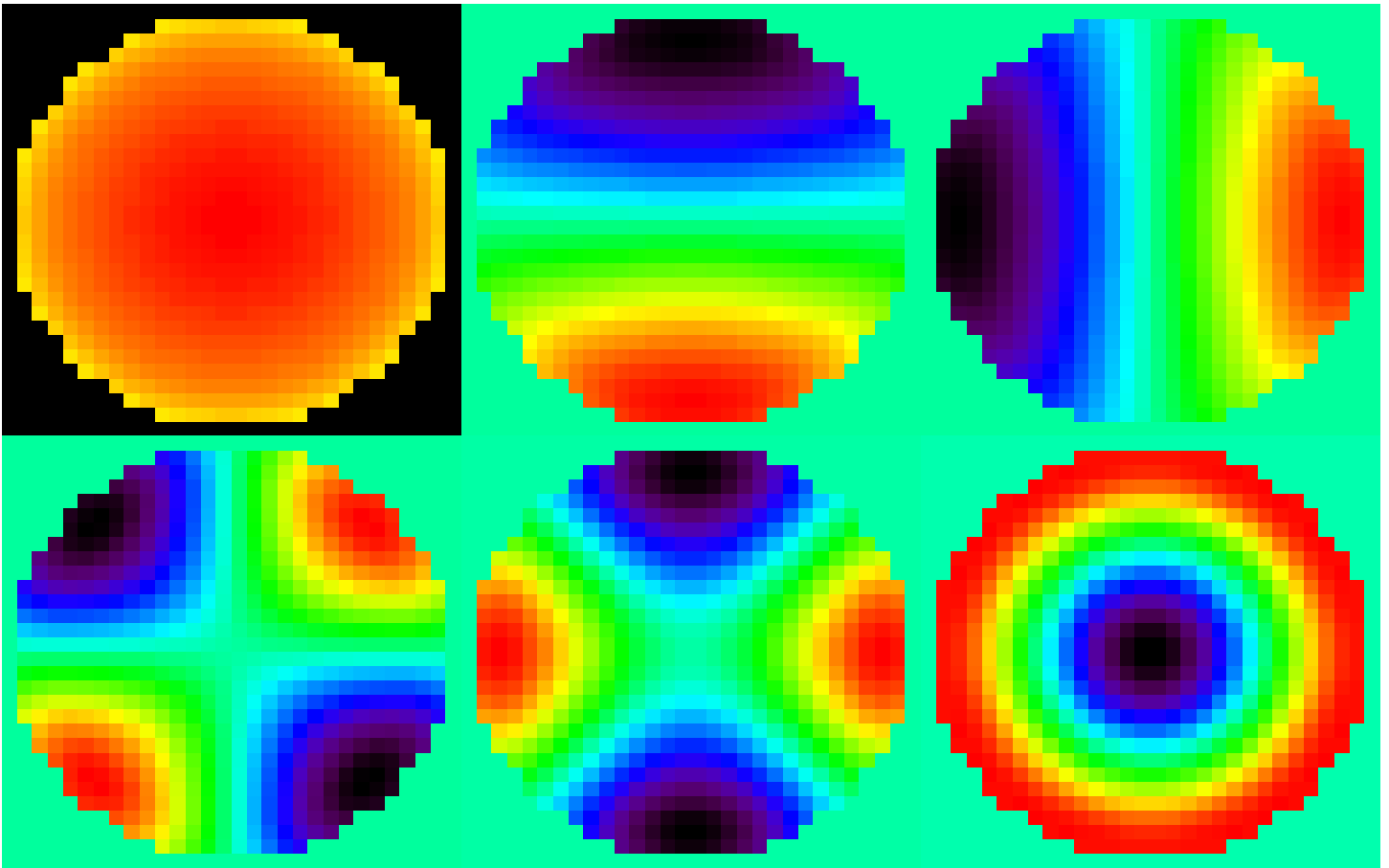
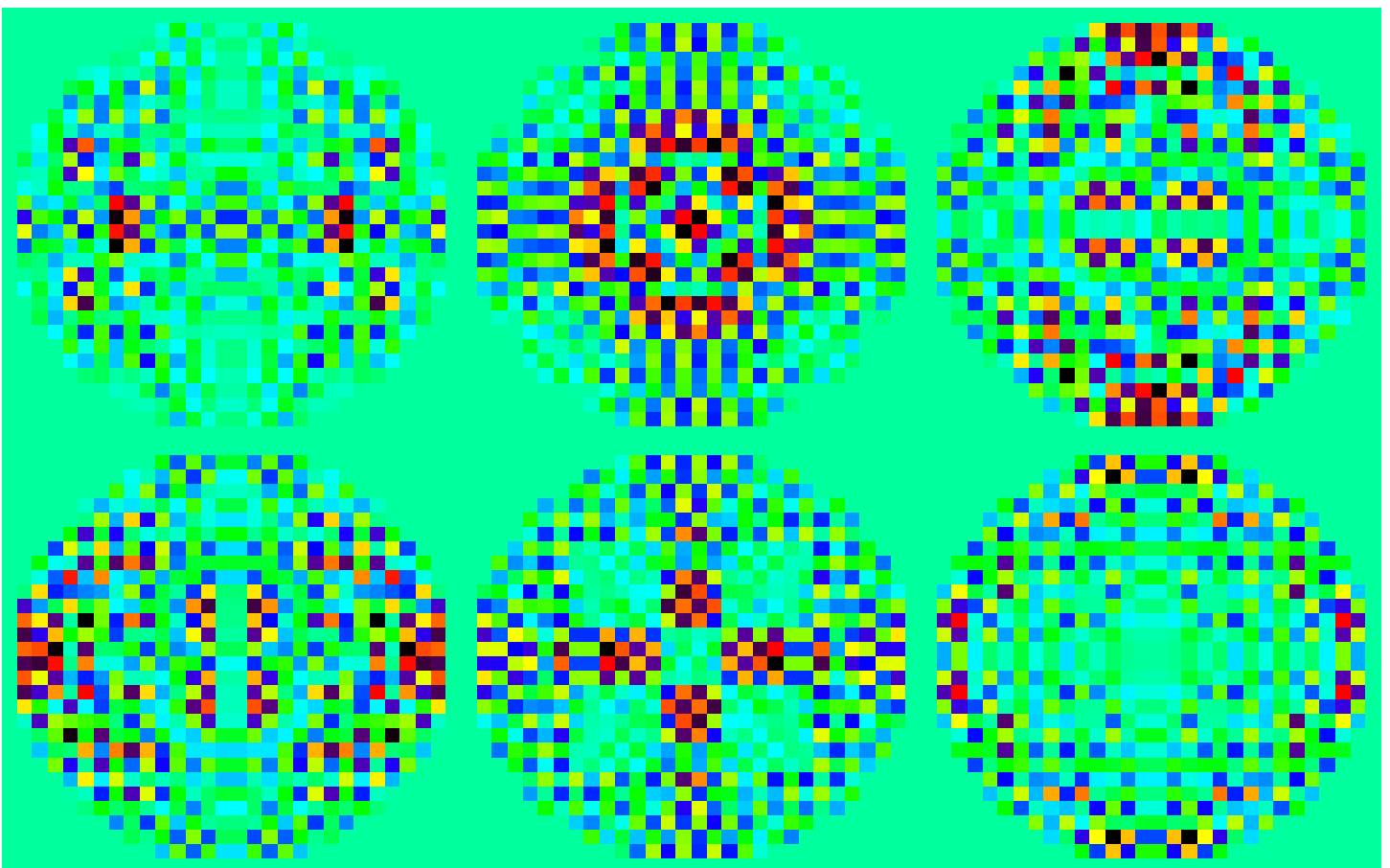


Figure 6 a): "Best" eigenvectors of the matrix shown in Figure 3. See text for color scale.



b): "Worst" eigenvectors



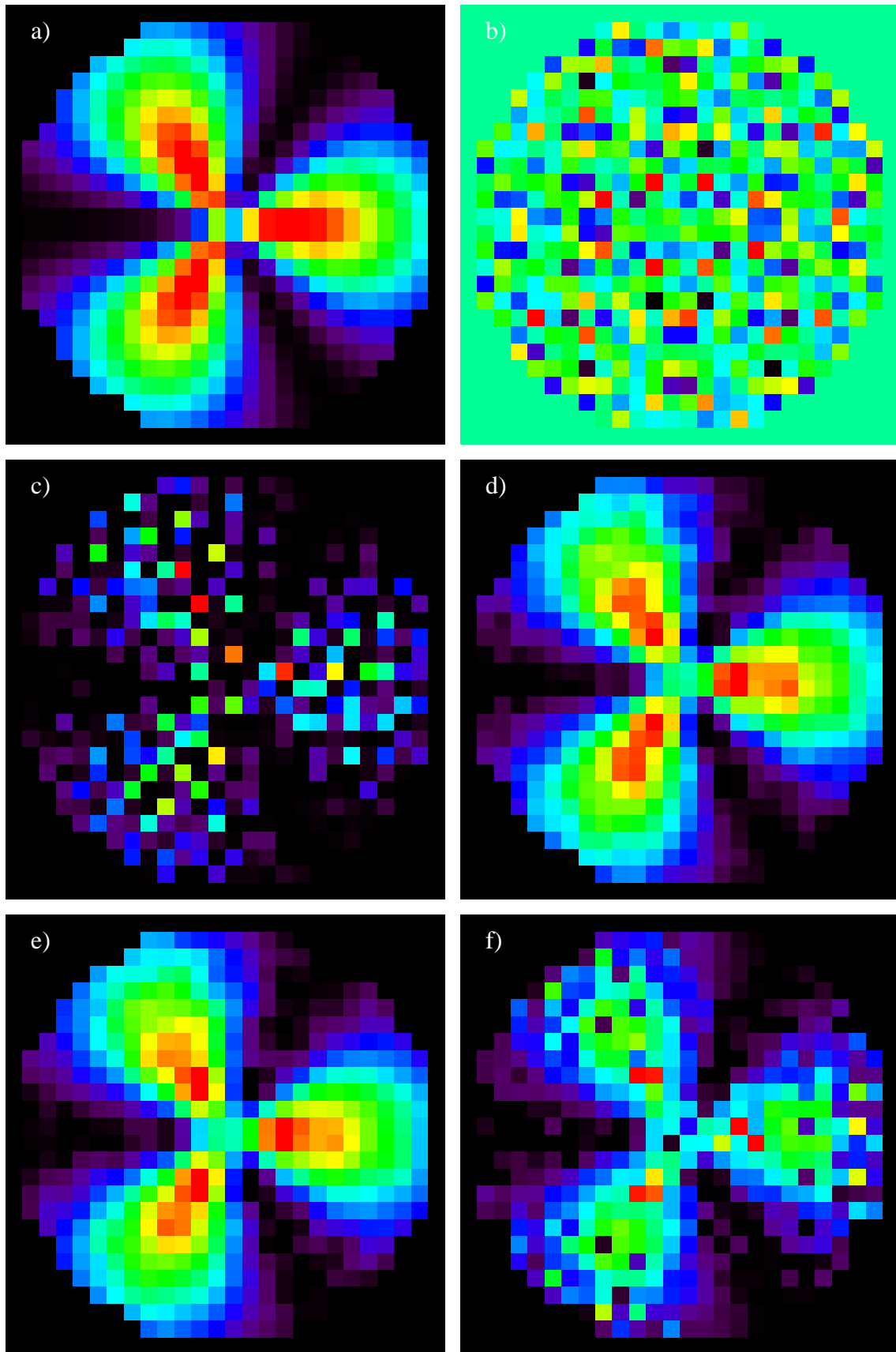


Figure 7: Effect on reconstruction of successive removal of eigenvectors

- a) Test Pattern b) Reconstruction with no noise reduction
- c) Constrained optimization, all 476 vectors
- d-f) 239, 170, and 21 vectors retained, respectively

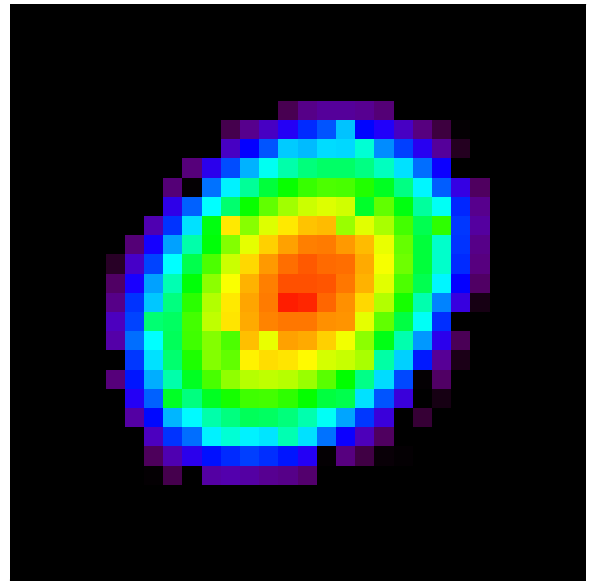
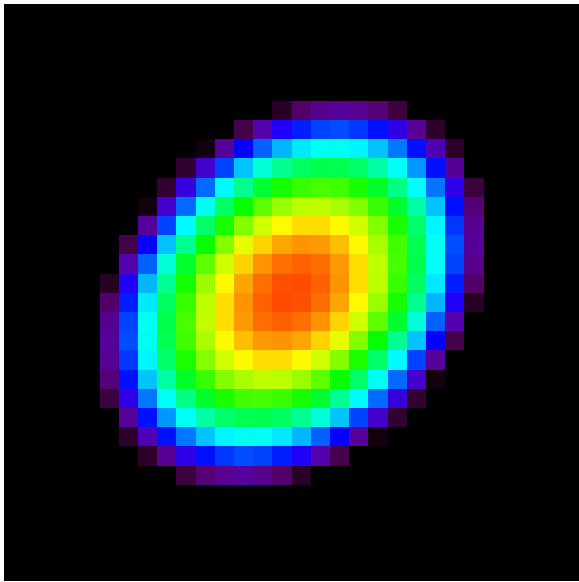
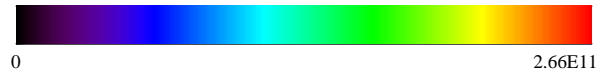


Figure 8: Example of reconstruction using best geometry

a) Test pattern

b) Reconstruction, yield = 1.2×10^{13}



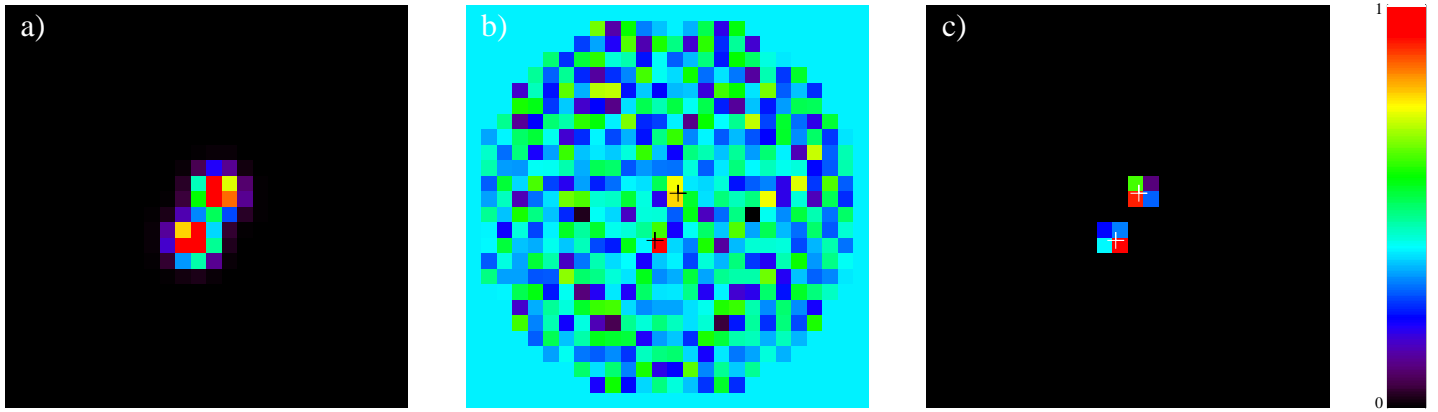


Figure 9: Artifacts caused by discretization

a) Image of point sources at arbitrary location b) Reconstruction c) Corrected

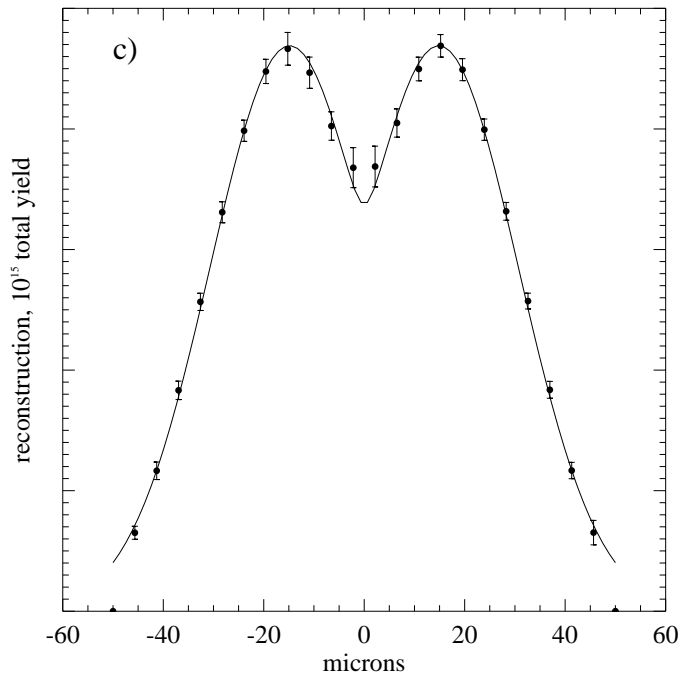
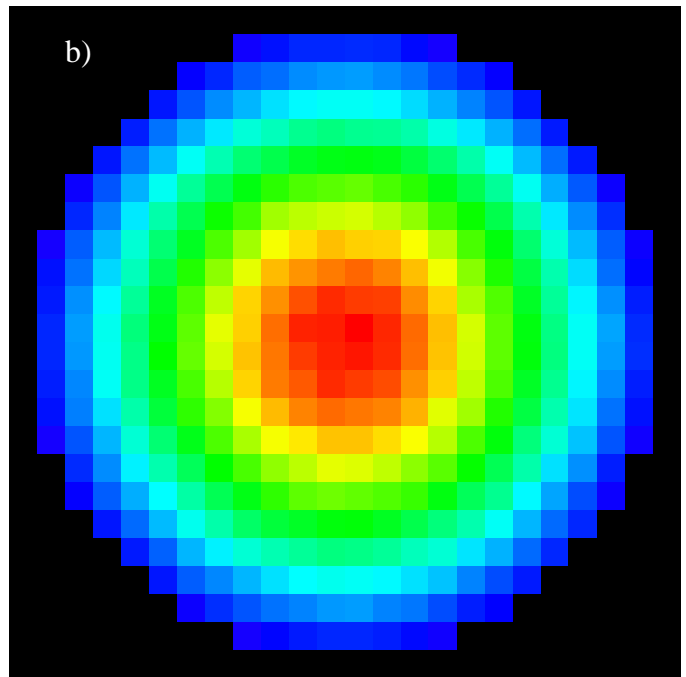
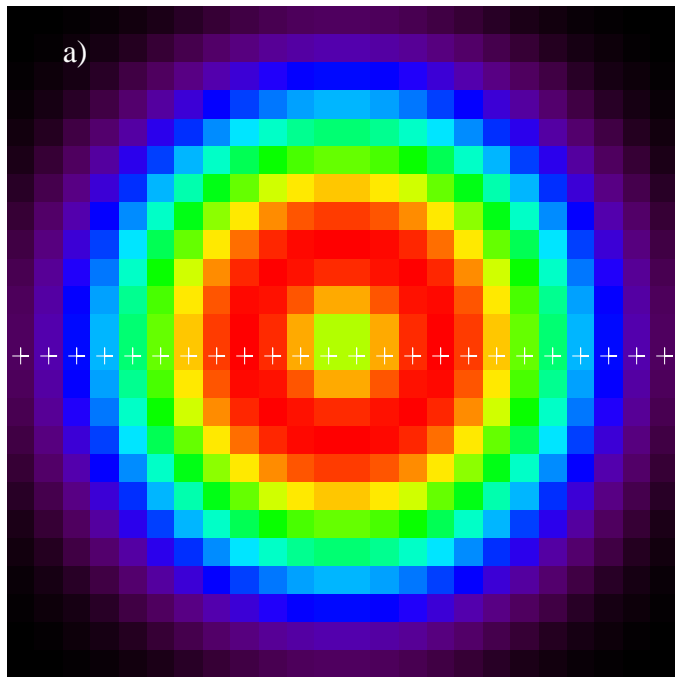


Figure 10: Quantification of errors caused by statistical noise
 a) test object, 10^{15} yield
 b) one of twenty noisy images
 c) reconstructions with error bars at positions of white crosses
 Solid line shows original object.
 The central dip is recovered, even though it is not visible in the images.

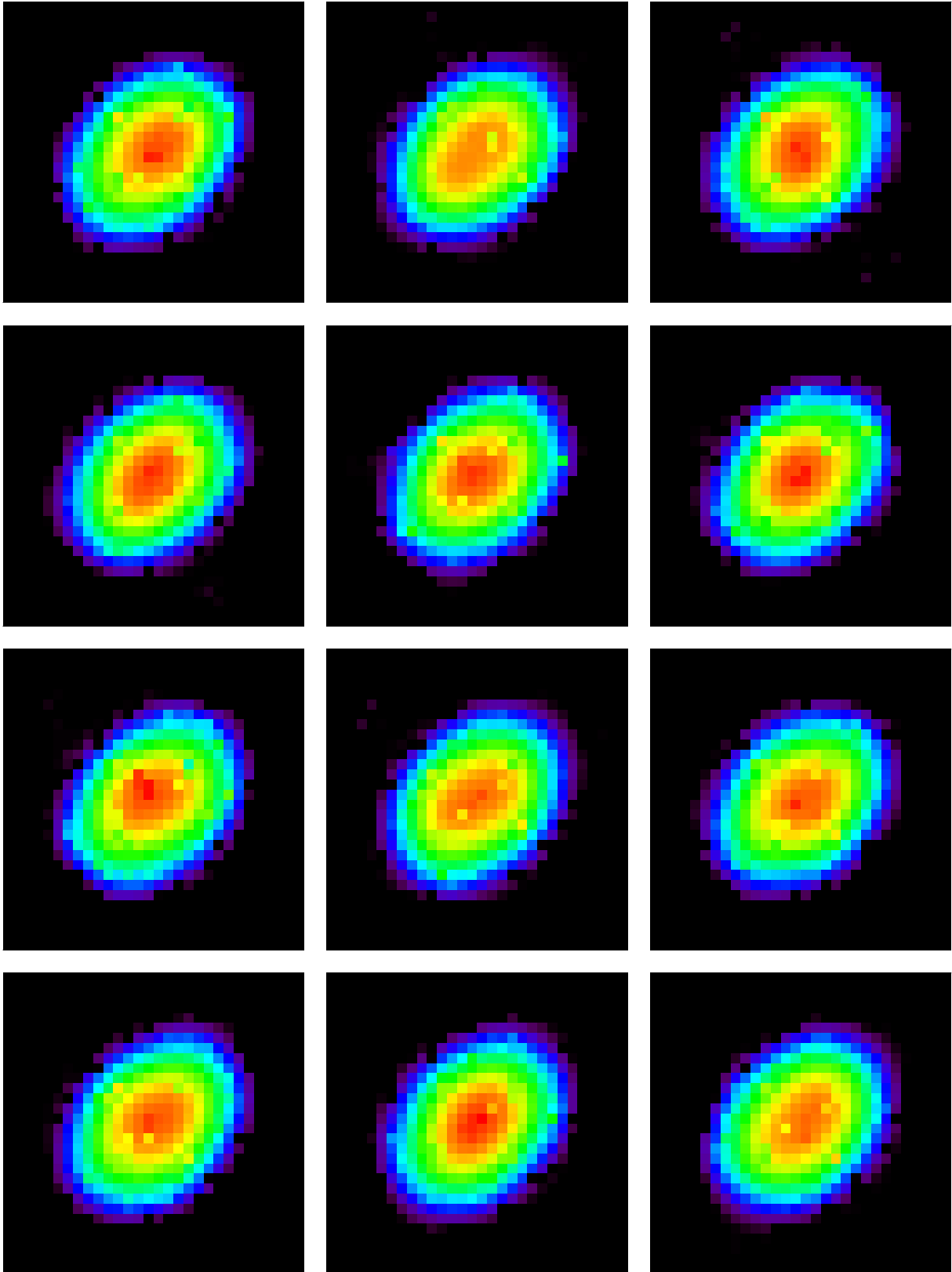


Figure 11: Reconstructions of twelve different noisy images, 1.2×10^{13} yield. The reconstructions are seen to be reliable.

